Article

Influence of the Thermal Processing and Doping on LaMnO$_3$ and La$_{0.8}$A$_{0.2}$MnO$_3$ (A = Ca, Sr, Ba) Perovskites Prepared by Auto-Combustion for Removal of VOCs

Natasha Di Benedetto [1], Carolina De los Santos [2,*], María Del Pilar Yeste [3], Jonder Morais [4], Maria Do Carmo Martins Alves [5], Alejandro Amaya [2], Leopoldo Suescun [1,*], José Manuel Gatica [3], Hilario Vidal [3] and Jorge Castiglioni [2]

[1] Laboratorio de Cristalografía, Química del Estado Sólido y Materiales, DETEMA, Facultad de Química, Universidad de la República, Av. Gral. Flores 2124, Montevideo 11800, Uruguay
[2] Laboratorio de Fisicoquímica de Superficies, Área Fisicoquímica, DETEMA, Facultad de Química, Universidad de la República, Av. Gral. Flores 2124, Montevideo 11800, Uruguay
[3] Departamento C.M. I.M. y Química Inorgánica, Universidad de Cádiz, 11510 Puerto Real, Spain
[4] Laboratório de Espectroscopia de Elétrons (LEe-), Instituto de Física, Universidade Federal do Rio Grande do Sul, Porto Alegre 91501-970, RS, Brazil
[5] Instituto de Química, Universidade Federal do Rio Grande do Sul, Porto Alegre 91501-970, RS, Brazil
* Correspondence: cdlsantos@fq.edu.uy (C.D.l.S.); leopoldo@fq.edu.uy (L.S.)

Abstract: Single-phase oxygen stoichiometric LaMnO$_3$ and doped La$_{0.8}$A$_{0.2}$MnO$_3$ (A = Ca, Sr, Ba) perovskites have been prepared by a simple one-step auto-combustion method. Cation-deficient LaMnO$_{3+\delta}$ and La$_{0.8}$A$_{0.2}$MnO$_{3+\delta}$ were obtained by calcination of the former samples in air at 750 °C. The samples were characterized by X-ray powder diffraction, X-ray photoelectron spectroscopy, temperature-programmed reduction, temperature-programmed oxygen desorption, and N$_2$ physisorption in order to apply them as catalysts in the complete catalytic oxidation of acetone as a model volatile organic compound. The studied phases show the expected orthorhombic and rhombohedral perovskite crystal structures. Catalytic experiments performed with all the samples show measurable activity already at 100 °C. At 200 °C, doped La$_{0.8}$A$_{0.2}$MnO$_3$ samples show higher activity than undoped LaMnO$_3$, with increasing conversion with larger A-cation size. Calcined samples also show higher activity than as-prepared ones making La$_{0.8}$Ba$_{0.2}$MnO$_{3+\delta}$ the best catalyst at this temperature. All doped samples show >95% acetone conversion at T $\geq$ 250 °C with a weak dependence on the sample processing or A cation doping. The collected evidence confirms that the most important factors for the catalytic activity of these oxides are the Mn^{4+}/Mn^{3+} molar ratio on the surface of the samples and the cation-deficiency of the bulk perovskite structure. In addition, increasing the symmetry of the bulk crystal structure appears to have an additional favourable effect. Despite the observation of the presence of surface carbonates, we show that it is possible to use the as-prepared samples without further thermal treatment with good results in the oxidation of acetone.

Keywords: VOC; perovskites; catalytic oxidation; acetone; auto-combustion synthesis

1. Introduction

Noble metal-based catalysts have a high activity for the oxidation of most volatile organic compounds (VOCs). However, they are relatively expensive and tend to be de-activated by coking, poisoning, thermal sintering, etc. [1]. Therefore, the design and development of new materials with high performance, low cost, chemical and thermal stability at the operation temperature and high tolerance to catalytic poisons, is increasingly pursued [2–8]. Transition metal oxides, especially perovskite manganites, are among the best catalysts tested for VOCs oxidation at low temperatures [6]. Catalytic activity of manganites can be generally attributed to the redox properties of manganese, showing mixed-valence states, the high mobility of oxygen within the crystal structure and the

presence of adsorbed oxygen species [9–17]. $LaMnO_{3+\delta}$ perovskite has been evaluated for total oxidation of toluene [18–20], methanol [19], benzene [21], propane [22], methane [23], hexane [24], acetone [8] and chlorinated compounds [25,26], among others. The modification of $LaMnO_3$ through doping at the A-site by different species has been used to increase the activity of the catalyst [16,27].

When prepared in air at high temperatures, $LaMnO_3$ forms the metal-vacant phase $La_{1-\varepsilon}Mn_{1-\varepsilon}O_3$ of rhombohedral symmetry ($R\bar{3}c$ space group), usually described as $LaMnO_{3+\delta}$ [28–31]. A similar effect has been described for low-doped $(La_{0.8}A_{0.2})MnO_3$ (A = Ca, Sr, Ba) forming $(La_{0.8}A_{0.2})_{1-\varepsilon}Mn_{1-\varepsilon}O_3$ also usually described as $La_{0.8}A_{0.2}MnO_{3+\delta}$ [31] where δ represents excess oxygen respect to the metals, but not interstitial oxygen. These metal-vacant phases are stabilized by the oxidation of Mn^{3+} into Mn^{4+} in the presence of oxygen at moderate-to-high temperatures achieving equilibrium with maximum δ = 0.26 for $LaMnO_3$ annealed at 1000 °C in O_2 [29]. Preparation of oxygen-stoichiometric $LaMnO_3$ containing pure Mn^{3+} and $La_{0.8}A_{0.2}MnO_3$ containing up to 20% Mn^{4+} was usually achieved by firing non-stoichiometric phases at high temperature and low oxygen-partial-pressure atmosphere [28–31], observing a change in the symmetry of the perovskite structures from the metal-vacant rhombohedral $R\bar{3}c$ structure to the stoichiometric orthorhombic *Pbnm* structure. Reports that have shown rhombohedral $LaMnO_{3+\delta}$ and A-doped $LaMnO_3$ catalytic activity for oxidation of VOCs generally make no mention of the oxygen/metal stoichiometry calling them $LaMnO_3$ and $La_{1-x}A_xMnO_3$ [5,7,10,18–22,24,25,32–34]. Recent reviews on the use of perovskites in the catalytic oxidation of different VOCs have not investigated the relative effect of changing the oxygen stoichiometry or A-site dopant in the catalytic activity [4,5,27].

In this work, stoichiometric $LaMnO_3$ and alkaline-earth substituted $La_{0.8}A_{0.2}MnO_3$ (A = Ca, Sr, Ba) perovskites were prepared by a modified auto-combustion method. They were characterized and tested as catalysts in the complete catalytic combustion of acetone (chosen as model VOC). The cation-deficient rhombohedral $LaMnO_{3+\delta}$ and alkaline-earth substituted $La_{0.8}A_{0.2}MnO_{3+\delta}$ phases were also tested in identical conditions for comparison purposes. The effects of different metals substitution (A) and initial oxygen stoichiometry (δ) in the catalytic activity over several catalytic cycles are discussed.

2. Results

2.1. Structural Characterization

The auto-combustion synthesis method used in this work yields perovskite phases in one synthesis step. The as-prepared samples obtained were orthorhombic $LaMnO_3$ (LM) and $La_{0.8}Ca_{0.2}MnO_3$ (LCM), and mixed-phase orthorhombic and rhombohedral $La_{0.8}Sr_{0.2}MnO_3$ (LSM) and $La_{0.8}Ba_{0.2}MnO_3$ (LBM) (Figure 1) corresponding to oxygen-stoichiometric samples as described in [28–31]. ICP-AES spectroscopic results obtained for these samples (Table S1) indicate that La, Mn and A cations fall in the expected composition range within experimental uncertainty, considering the presence of ~1% weight from carbonated species (see discussion in Sections 2.7 and 3 and Supplementary Materials), confirming the adequacy of the preparation method to obtain the desired perovskite phases. These phases correspond to bulk stoichiometric perovskites, showing no significant amount of cation vacancies. The change in the symmetry observed in doping is caused by the change of ionic radii of the A cation as predicted by the Goldschmidt tolerance factor in $AMnO_3$ perovskites [35,36]. The calcined samples show different symmetry relative to the as-prepared compounds at room temperature. They are orthorhombic $La_{0.8}Ca_{0.2}MnO_{3+\delta}$ (LCM750), rhombohedral $LaMnO_{3+\delta}$ (LM750), $La_{0.8}Sr_{0.2}MnO_{3+\delta}$ (LSM750) and biphasic rhombohedral and cubic $La_{0.8}Ba_{0.2}MnO_{3+\delta}$ (LBM750) (Figure 1). For all the samples studied, no additional unexplained diffraction peaks could be detected, (except for one peak assigned to $CaCO_3$ in the as-prepared LCM sample), confirming that the samples are >99% pure with respect to crystalline phases for LM, LSM and LBM and >95% pure for LCM. Note that amorphous phases in small proportions and crystalline phases below 1% weight show, in general, no detectable signal in a conventional XRD diffractogram. Rietveld plots, final refined unit cell parameters of the observed phases and fit agreement parameters

are shown in Figures S1 and S2 as well as in Table S2. The results of the thermo-diffraction experiments are discussed in the following section.
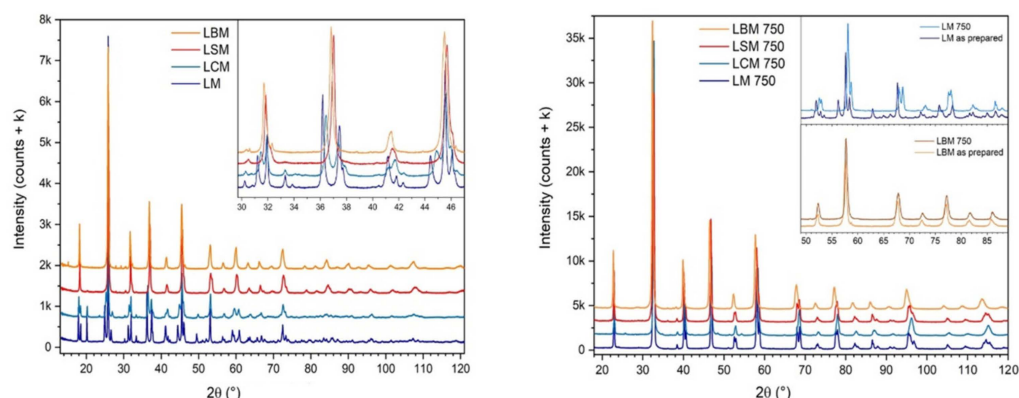

Figure 1. Conventional X-ray powder diffractograms of the LM, LCM, LSM and LBM as-prepared manganites and the LM750, LCM750, LSM750 and LBM750 calcined samples. Note that symmetry differences in the as-prepared samples are evidenced by the different number and positions of diffraction peaks, especially for LM and LCM, while all calcined samples show the same number of peaks as expected for the presence of rhombohedral phases (see respective insets).

2.2. Catalytic Performance

Acetone conversion (%) vs. temperature (°C) curves for the as-prepared and the calcined manganites are shown in Figure 2. At 100 °C, both groups of samples present similar conversion but at 150 °C the effect of A doping in the samples can be observed. Conversion values of LCM, LSM and LBM are at least 10% larger than that of LM between 150 °C and 250 °C, with a maximum difference of 20% for LCM at 150 °C. Similarly, conversion values of LCM750, LSM750 and LBM750 are at least 20% larger than those of LM750, with a maximum difference of 40% for LBM750 at 200 °C. Samples doped with Sr and Ca show similar catalytic activity both in the as-prepared or calcined form in the whole temperature range, while barium doping produces higher conversions above 150 °C. Conversion of acetone is larger than 95% for all doped samples below 250 °C. By observing the light-off curves in more detail one can see that all the calcined samples show a higher conversion of acetone between 150 °C and 250 °C with respect to the as-prepared ones.
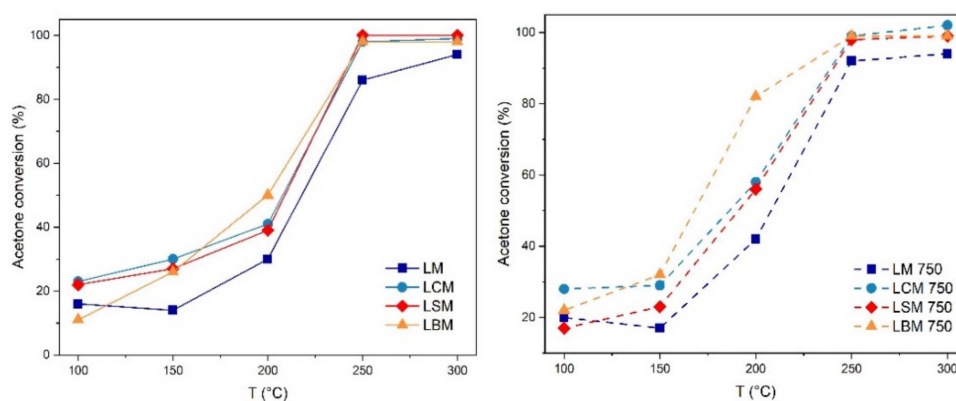
Figure 2. Acetone conversion vs. temperature curves for the LM, LCM, LSM and LBM as-prepared manganites and the LM750, LCM750, LSM750 and LBM750 calcined samples.

Figure 3 shows the light-off curves corresponding to five catalytic cycles carried out on the as-prepared samples in comparison with the respective calcined samples. For the LM sample, as the catalytic cycles are carried out, there is no noticeable difference in the percentage of acetone conversion, and they are similar to the calcined sample. LM750 sample was also cycled four times and neither shows a significant change in catalytic

activity over cycling (as shown in Figure S3). The LCM sample shows no clear trend of conversion over cycling, reaching values similar to those obtained for LCM750 in the best cycle. When the LSM sample is studied, it is observed that, as the cycles are carried out, the percent of acetone conversion increases, reaching the corresponding value of LSM750 conversion after four cycles. When five cycles are carried out for LBM, it is also observed that there is no variation in the acetone conversion, but these values differ from those obtained for the LBM750 sample with a maximum of 30% difference in acetone conversion at 200 °C.
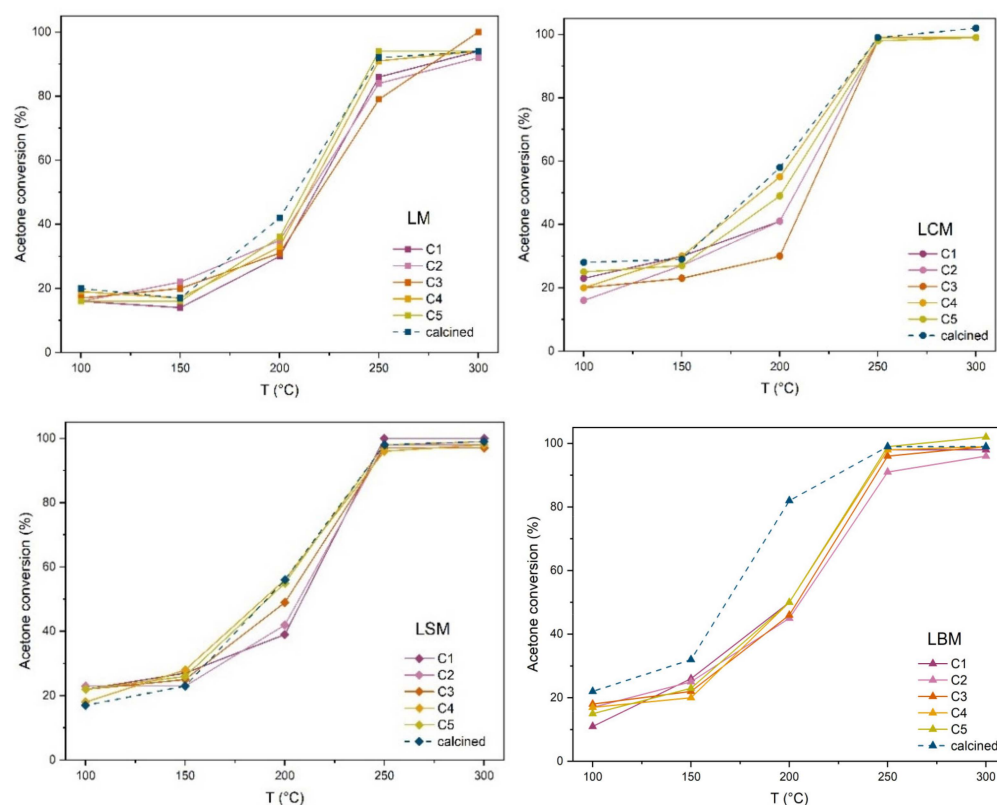

Figure 3. Acetone conversion of LM, LCM, LSM and LBM over five consecutive cycles compared with conversion of LM750, LCM750, LSM750 and LBM750.

Between 150 °C and 200 °C, the activation of the oxidation reaction occurs as CO_2 starts to be detected (Figure S4). At 150 °C, the formation of acetic acid is observed for all the samples tested. We define r as the ratio of $[CO_2]_{experimental}/[CO_2]_{theoretical}$. For most of the doped samples already at 250 °C, an r of 0.9 is reached, except for LCM and LCM750, which show an r of 0.87 and 0.75 respectively, detecting acetaldehyde as a by-product.

It is important to note that any change in the surface of the as-prepared samples will make them similar to the calcined ones because it will introduce the formation of metal vacancies at catalytic conditions. This surface modification may not be visible by X-ray powder diffraction, since the technique is more sensitive to the bulk structure. However, all the as-prepared samples start showing indications of the transformation from orthorhombic to rhombohedral phase between 200 °C and 300 °C on heating. Orthorhombic perovskite oxides usually transform reversibly to rhombohedral ones on heating [35] due to changes in the Goldschmidt tolerance factor. However, in this case, this effect is irreversible as it is mainly caused by the gain of oxygen, as depicted in Figure 4 for LBM (and Figure S5 for LM, LCM and LSM). We hypothesize that the as-prepared, stoichiometric samples show similar or slightly less activity than the calcined catalysts, but become quickly oxidized at the surface above 200 °C in the presence of O_2. This makes the activity of all the samples above 200 °C similar to the activity of the rhombohedral/cubic phases showing cation vacancies. Note that the LBM750 sample shows rhombohedral and cubic perovskite phases

at room temperature (Figure 1). The proportion of cubic $La_{0.8}Ba_{0.2}MnO_{3+\delta}$ increases at higher temperatures, which improves oxygen mobility [37].
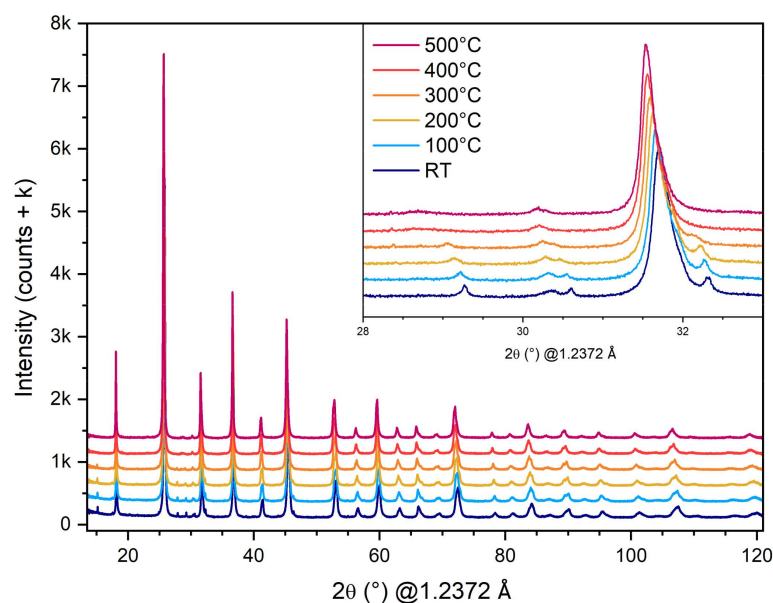

Figure 4. Synchrotron XRD patterns of the as-prepared LBM sample heated from RT to 500 °C in air. Note that the peaks at ~29° and ~32° (inset) almost disappear at 300 °C indicating the oxygen uptake with the formation of cation vacancies and transformation of the orthorhombic to rhombohedral phase.

Table 1 shows the temperature values for conversions of 50% (T_{50}) and 80% (T_{80}) of acetone. For all the compositions tested, there are two general trends. There is a reduction in both temperatures with the size of the A cation, and the same is observed with calcination.

Table 1. Estimated temperature values (°C) for acetone conversions of 50 and 80% for the as-prepared and calcined samples.

Catalyst	T_{50} [°C]	T_{80} [°C]
LM	218	244
LM 750	208	238
LCM	208	235
LCM 750	190	227
LSM	209	234
LSM 750	193	228
LBM	200	231
LBM 750	168	198

2.3. TPR

TPR measurements are shown in Figure 5 and the calculated amounts of consumed hydrogen from TPR profiles are summarized in Table 2. For all the studied samples, two reduction stages are observed in the TPR profile, one below 600 °C and the other at around 800 °C. Owing to the fact that La^{3+}, Sr^{2+}, Ca^{2+} and Ba^{2+} are not reducible under the measurement conditions, the water production is due to the reduction of manganese. According to the literature [38–40], the H_2 consumption below 600 °C corresponds to the reduction of Mn^{4+} to Mn^{3+} while that observed at high temperature it is attributed to the reduction of Mn^{3+} to Mn^{2+} (which will not be discussed because it is beyond the

temperature range considered for the reaction conducted under oxidizing conditions in this work).
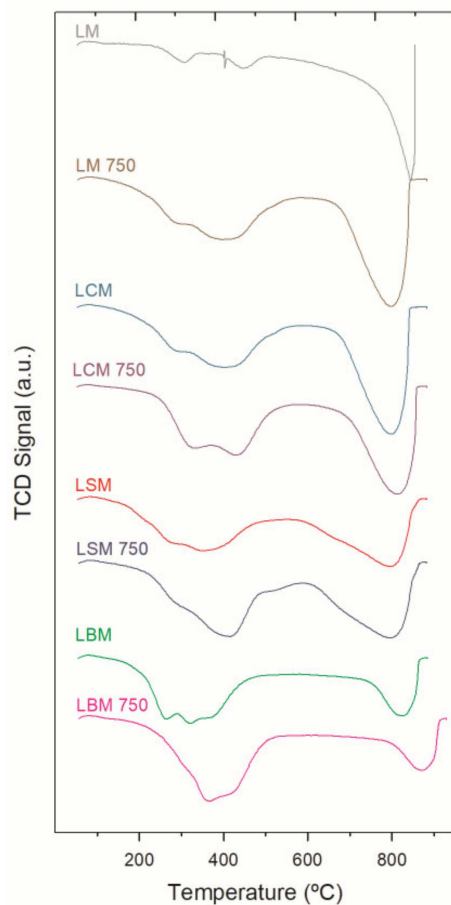

Figure 5. H_2-TPR curves of the studied samples.

Table 2. Reducibility of perovskite samples.

Catalyst	H_2 Uptake (mol H_2 mol^{-1} cat.)		
	T $\leq$ 600 °C	T > 600 °C	Total
LM	0.04	0.35	0.39
LM 750	0.23	0.42	0.65
LCM	0.18	0.34	0.52
LCM 750	0.25	0.32	0.57
LSM	0.25	0.28	0.53
LSM 750	0.29	0.28	0.57
LBM	0.30	0.24	0.54
LBM 750	0.32	0.25	0.57

Then, based on the first reduction process (Table 2), it is possible to obtain the Mn^{4+} content of the perovskite being the 100% of Mn^{4+} equal to 1/2 mol H_2 mol^{-1} cat.

The doping of the perovskite leads to an increase in the Mn^{4+} content in the perovskite structure, rising from 4% Mn^{4+} in LM to 30% in the case of the Ba-doped sample. Moreover, the calcination treatment also increases the Mn^{4+} content for all the samples.

2.4. O₂-TPD

The results of O$_2$-TPD analysis are presented in Figure 6. Evolved oxygen can be categorized as β-oxygen, which is ascribed to the bulk crystal structure oxygen in the perovskite framework [41,42]. In LM perovskite containing more than 95% of Mn^{3+}, no oxygen removal is observed. For LCM, LSM and LBM, containing only ~20% of Mn^{4+} a peak starting around ~300 °C is detected for all the as-prepared samples (characterized by two broad features in LCM), probably related to the reduction of all Mn^{4+} to Mn^{3+} with the formation of oxygen-deficient perovskites (δ < 0 in La$_{0.8}$A$_{0.2}$MnO$_{3+\delta}$). After the calcination treatment, which introduces cation vacancies in the perovskite, the four compounds show release of oxygen starting above 450 °C. The semi-quantitative nature of this technique prevents the correlation between peak areas and the amount of oxygen removed, as observed in LSM and LSM750 where the opposite area relation is observed with respect to the rest of the samples. The temperature of the processes is clearly the same for the three as-prepared A-doped samples and the four calcined samples. Bulk studies indicate that the heating treatment performed on the as-prepared perovskites generates a net oxygen gain and consequently an increase in the Mn^{4+}/Mn^{3+} ratio, which can be correlated with the improvement in the catalytic response of the calcined samples.

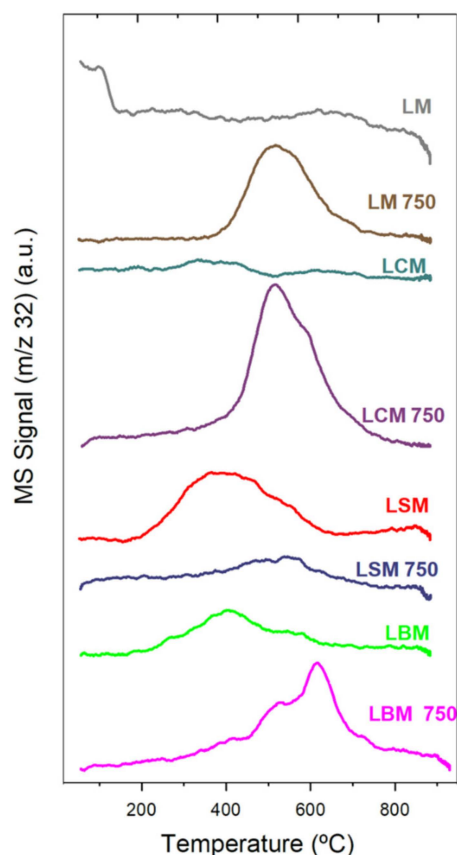**Figure 6.** O$_2$-TPD diagrams of the studied samples.

2.5. Textural Properties by Means of N₂ Physisorption

Nitrogen physisorption isotherms for LBM and LBM750 are shown in Figure 7 (and Figure S6 for LM, LCM and LSM). According to the IUPAC classification, the curves in the figure correspond to type II. This is characteristic of low-porous or macroporous solids. In LBM, a very light hysteresis (H3 type, Boer) is perceived, which could indicate the presence of lamellar solids. For LBM750, the hysteresis effect disappears, denoting a slight modification in the porosity of the sample during the calcination process used to transform LBM into LBM750. This behaviour is similar in all the doped samples. The quantitative results of textural properties obtained for the as-prepared and calcined manganites are

shown in Table 3. It is observed that both types of samples have similar specific surface areas (S_{BET}), with low values of area per gram, but comparable to those reported in the literature for other perovskites prepared by other methods [11,13,32,41]. A small decrease in the specific area can be observed when samples are subjected to calcination except for LCM750, where the area seems to slightly increase despite having a similar total pore volume (V_{total}).
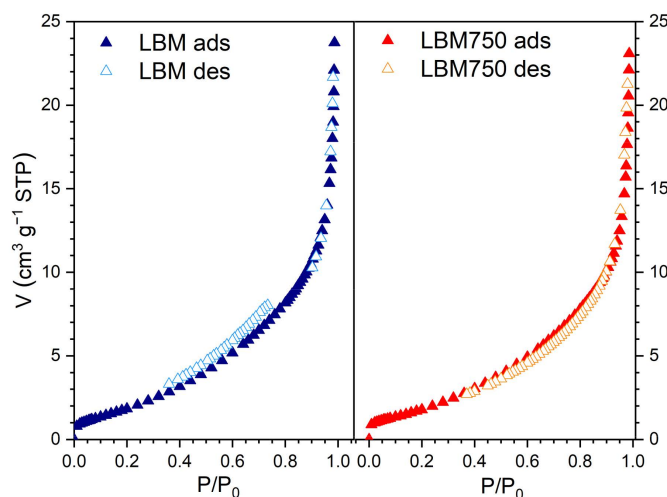

Figure 7. N_2 physisorption isotherms for LBM and LBM 750 samples.

Table 3. Textural properties for as-prepared and calcined manganites.

Catalyst	S_{BET} $[m^2g^{-1}]$	V_{total} $[m^3g^{-1}]$
LM	5.7	0.025
LM750	4.7	0.015
LCM	5.0	0.030
LCM750	6.9	0.030
LSM	7.0	0.030
LSM750	5.5	0.030
LBM	7.1	0.030
LBM750	6.7	0.030

2.6. SEM-EDS Characterization

SEM micrographs show an apparently homogeneous surface of all the samples (Figure 8). In order to determine the presence of significant impurities, the X-ray emission spectra (EDS) of different points on the surface of each sample, showing different aspects from the average, were collected and qualitative analysis of metals was performed. This can be observed in Figures S7–S14 where the micrograph and spectra of each marked point are shown. The variations in metal composition (as extracted from the area of peaks of each phase) suggest that there is no phase segregation. Notice that no region shows a significant excess/defect of one metal, as would correspond to the presence of separated La, Ca, Sr, Ba or Mn carbonates (as suggested in the following section) and all the metals La, Mn and A (when adequate) could be observed at every point selected as shown in Tables 4, S3 and S4. In addition, the SEM-EDS study allows ruling out the presence of large granular impurities on the surface of all the samples.
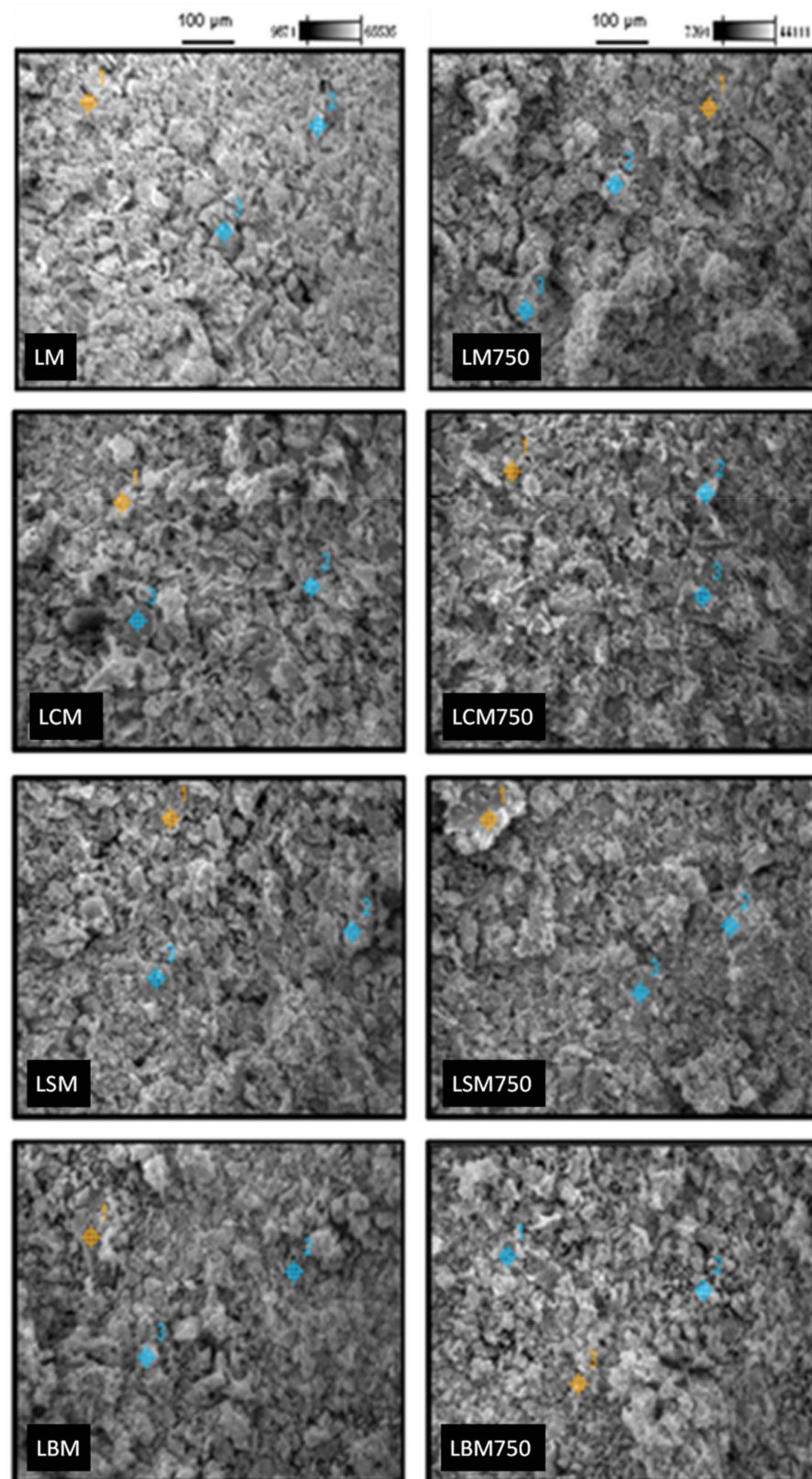
Figure 8. SEM images of the studied samples. EDS analysis points allowing the elemental % data gathered in Table 4 are indicated.

Table 4. Atom % obtained by EDS corresponding to the points indicated in the SEM images shown in Figure 8.

Sample	Atom %			Sample	Atom %		
	O	**Mn**	**La**		**O**	**Mn**	**La**
LM	60.4	18.4	20.1	LM750	61.5	17.1	19.3
	44.3	23.6	30.4		37.9	25.0	36.7
	63.2	17.0	18.1		58.3	18.4	21.3
LCM	69.2	14.0	12.5	LCM750	57.5	19.2	18.2
	60.0	19.3	15.7		62.0	17.4	14.1
	48.6	24.4	19.8		61.5	18.3	14.7
LSM	62.6	18.0	13.6	LSM750	71.2	12.7	11.8
	66.9	14.6	12.9		67.8	14.8	11.4
	59.9	20.0	14.0		65.3	14.9	13.9
LBM	58.7	18.2	16.2	LBM750	67.6	14.2	13.4
	66.0	15.2	12.0		61.9	16.6	14.7
	66.1	15.6	12.7		69.4	14.3	11.0

2.7. XPS Characterization

XPS measurements provide the chemical environment of the atoms present on the outmost layers of the samples. Table 5 displays the surface composition (atom %) of all samples as calculated from the XPS survey scans. It is clear that, besides the expected elements present in the expected ratios, the samples also have considerable surface carbon content. This was expected based on the synthesis method and sample storage in air, as will be discussed in the next section. The Mn 2p XPS spectra (see Figure 9) are especially relevant for this study and presented similar features for all samples. They show the presence of both Mn^{3+} and Mn^{4+} oxidation states on the surface [42], although identification of the specific chemical bonds associated with them is difficult from the Mn 2p signal. This difficulty is due to the very similar binding energy values for several Mn bonds, such as oxides. In the LM sample, the Mn^{4+}/Mn^{3+} ratio is the lowest and Mn^{3+} cations dominate, as expected for a sample with bulk Mn^{3+} oxidation state. The Mn^{4+}/Mn^{3+} ratio increases with the A doping and with calcination for the same sample, also expected from the formation of bulk metal-deficient samples with the shift of Mn average charge closer to Mn^{4+}. The presence of carbon in the form of carbonates justifies the observation of $CaCO_3$ in the LCM sample and of carbonated species in the La $3d_{5/2}$, Ca 2p, Sr 3d, and Ba $3d_{5/2}$ region fits (Figures S15 and S16) [43]. Since La, Ca, Sr and Ba are generally considered spectators in the catalytic activity of these manganites, the detailed analysis of the spectra for each of the elements in each sample is given in the Supplementary Materials (Figures S15 and S16).

Table 5. Surface atomic concentrations (%) determined from the XPS survey spectra and Mn cations ratios for each sample, being A the dopant element.

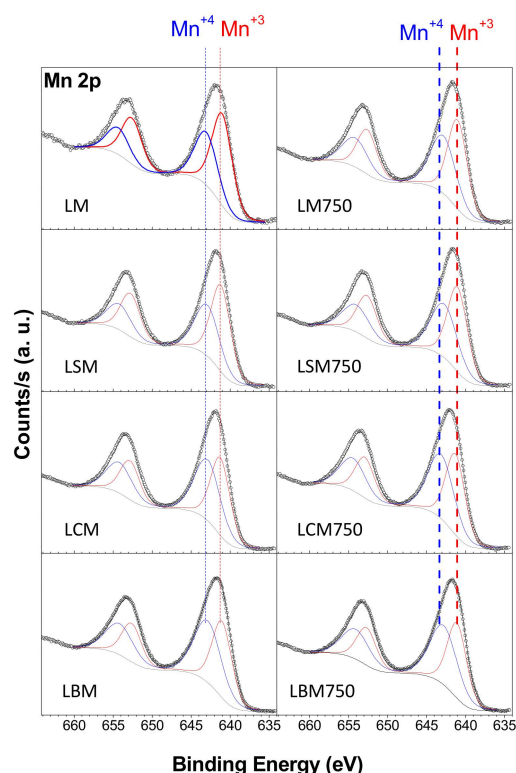| Sample	A	Element (Atom %)				
		O	**Mn (Mn^{4+}/Mn^{3+} Ratio)**	**La**	**C**	**A**
LM	-	48.9	6.9 (0.6)	4.4	39.8	-
LM750	-	46.3	8.1 (0.8)	5.1	40.5	-
LCM	Ca	49.7	8.5 (1.0)	4.4	32.7	4.7
LCM750	Ca	49.4	10.2 (1.1)	5.7	31.2	3.5
LSM	Sr	50.0	8.6 (0.7)	4.2	35.5	1.7
LSM750	Sr	47.8	8.9 (0.8)	4.2	37.6	1.5
LBM	Ba	45.9	7.4 (1.1)	3.8	41.2	1.7
LBM750	Ba	47.6	9.3 (1.1)	4.4	36.0	2.7

Figure 9. Mn 2p XPS spectra (dots) for all as-prepared and calcined samples fitted with two chemical states named Mn^{4+} (blue lines) and Mn^{3+} (red lines).

3. Discussion

All results obtained from the bulk and surface characterization techniques applied to the as-prepared and calcined materials are consistent with the presence of perovskite manganites containing bulk Mn^{3+} in the case of as-prepared $LaMnO_3$ (LM) and Mn^{3+}/Mn^{4+} mixtures for the rest of the doped (LCM, LSM, LBM) and calcined (LM750, LCM750, LSM750 and LBM750) samples. All the samples show the expected crystalline structures consistent with thermal treatment and oxygen content, with no indication of the presence of crystalline impurities, except for a small amount of $CaCO_3$ in LCM. The hydrogen consumption and oxygen evolution behaviour in programmed reduction/desorption studies are also consistent with the aforementioned characteristics. XPS spectra show the expected chemical complexity of the grain surface, also observed by SEM, with the presence of similar amounts of carbon species in all the samples. The preparation procedure of LM, LCM, LSM and LBM implies the combustion of acetates and amine species in an open atmosphere and is expected to produce carbonates of the metals. All the samples were stored in 30 cm^3 Falcon tubes, therefore also exposed to atmospheric carbon during handling between the preparation and characterization steps. The similar carbon content in all the samples is consistent with carbonates or atmospheric carbon since La, Ca, Sr and Ba carbonates have been reported to be stable beyond the calcination temperature [44–47]. This is also confirmed by XPS results shown in Table 5.

EDS measurements provide additional evidence that there is no significant La/A/Mn segregation in the surface of the sample (see Figures S7–S14) expected for carbonate crystallization. In any case, these surface carbon species seem to have no detrimental effect on the catalytic properties of the material. The bulk stability of the materials has already been demonstrated. The comparable catalytic activity of as-prepared and calcined materials in this study shows they are good candidates either for systems that may use the raw catalysts without processing or require further processing (such as pre-formation of the catalyst, deposition to prepare supported catalysts and/or thermal treatments) since we

found that calcination in air maintains or slightly increases, in general, the catalytic activity of the samples.

The doping of LaMnO$_3$ (LM) with larger Ba^{2+} and Sr^{2+} cations generates higher symmetry structures with larger Mn^{4+} content due to the decrease of the charge of the A site and the reduction of the tilt of MnO$_6$ octahedra. This change has a beneficial effect on the catalytic response. La$_{0.8}$Ba$_{0.2}$MnO$_3$ sample shows the best conversion of acetone among the as-prepared samples. This may be a consequence of the change in the proportion of rhombohedral and cubic perovskite phases. At higher temperatures, the proportion of cubic La$_{0.8}$Ba$_{0.2}$MnO$_{3+\delta}$ increases, improving the oxygen mobility and thus the catalytic response. Calcination of the samples introduces cation vacancies in the structure, which also increase Mn^{4+} and oxygen content respect to the stoichiometric samples. This also improves the catalytic conversion of acetone for all the sample compositions studied. It is reported that the oxidation of hydrocarbons on perovskites occurs by means of a mechanism in which the VOC interacts with the oxygen present in the catalyst. The active oxygen content is directly related to the amount of cation vacancies [48,49]. The slight variability of the catalytic response of as-prepared samples with cycling may be attributed to the incorporation of oxygen (consequently more Mn^{4+}) in the surface of the sample during the catalytic process, consistent with the effect of doping, calcination, and thermal evolution of the samples at the working temperature. This makes the calcined La$_{0.8}$Ba$_{0.2}$MnO$_{3+\delta}$ (LBM750) sample the best catalyst of the series. The Mn^{4+} content is, however, similar for all calcined samples on the surface, and the catalytic activity of all the materials (above 90% conversion at 300 °C), confirms their similarity regarding catalytic performance.

4. Materials and Methods

4.1. Catalysts Preparation

LaMnO$_3$ and La$_{0.8}$A$_{0.2}$MnO$_3$ (A = Ca, Sr, Ba), perovskites were synthesized via an auto-combustion route, using ethylenediaminetetraacetic acid (EDTA) as organic fuel and chelating agent, and ammonium nitrate as combustion promoter. The selected method, already used for the preparation of other perovskite oxides [37,50–52] has been modified to obtain the desired material in one step directly from the initial dissolution of metals in stoichiometric proportion. This method is cheap, fast (3–5 h total from weighing the reactants to the obtainment of the final sample), and scalable, since it allows us to obtain several grams (5–20 g) of the final material in one beaker.

For this purpose, aqueous solutions containing stoichiometric amounts of La(NO$_3$)$_3$·6H$_2$O, Sr(NO$_3$)$_2$, Ba(NO$_3$)$_2$, Ca(CH$_3$CO$_2$)$_2$·H$_2$O and Mn(CH$_3$CO$_2$)$_2$·4H$_2$O (>99.9%, Sigma-Aldrich, San Luis, MO, USA) were prepared according to the desired composition. An alkaline solution (pH = 10) containing 1.1 moles of EDTA (>99.4%, Sigma-Aldrich, San Luis, MO, USA) per mole of cation and NH$_4$NO$_3$ (>99.0%, Sigma-Aldrich, San Luis, MO, USA) was also prepared and the aforementioned solutions were mixed. EDTA molar excess ensures the total complexation of the cations. A 10:1 NH$_4$NO$_3$:EDTA molar ratio was chosen to promote the auto-combustion process. The resulting solution was heated over a hot plate at 130 °C, constantly stirring and keeping the pH constant (monitored every 30 min and restored to pH = 10 using small aliquots of NH$_4$OH), until the formation of a gel. Then, the magnetic stirrer was removed, and the temperature of the hot plate was raised to 300 °C, where the gel self-ignited [Safety note: Depending on the size of the beaker, the mass of reactants and the EDTA/NH$_4$NO$_3$ ratio, the auto-combustion process may produce ejected ashes or sparks falling outside the beaker. This procedure must be performed inside a hood and the surface should be free of flammable products around the hot plate]. The combustion process resulted in a sponge-like black powder, corresponding to the desired perovskite compounds, as confirmed by X-ray powder diffraction. The samples were ground in an agate mortar until a fine and homogeneous powder was obtained. After that, a portion of each sample was subjected to a heating treatment in a muffle furnace at 750 °C in air for 8 h to obtain the calcined samples. The samples obtained directly from the synthesis process, LaMnO$_3$, La$_{0.8}$Ca$_{0.2}$MnO$_3$, La$_{0.8}$Sr$_{0.2}$MnO$_3$ and La$_{0.8}$Ba$_{0.2}$MnO$_3$ (LM, LCM, LSM and LBM, respectively) denote the as-prepared samples, while

those obtained after the calcination process, $LaMnO_{3+\delta}$, $La_{0.8}Ca_{0.2}MnO_{3+\delta}$, $La_{0.8}Sr_{0.2}MnO_{3+\delta}$ and $La_{0.8}Ba_{0.2}MnO_{3+\delta}$, (LM750, LCM750, LSM750 and LBM750, respectively) are described as calcined.

4.2. Catalysts Characterization

4.2.1. Inductively Coupled Plasma Atomic Emission Spectroscopy

The metal contents in the as-prepared materials were determined by inductively coupled plasma atomic emission spectroscopy (ICP-AES) in an Iris Intrepid Thermo Scientific equipment. Three takes of each sample were prepared by acid digestion of a solution containing (2 to 3) mg of the material and Milli-Q water up to 0.05 L, in a Digestor Digiprep Jr. SCP-Science equipment. The results are consistent within uncertainty with the expected nominal formula including up to 1% weight of impurities such as carbonates, as discussed in Section 2.1.

4.2.2. X-ray Powder Diffraction

Conventional X-ray powder diffraction (XRD) measurements were performed over as-prepared and calcined samples in a Rigaku ULTIMA IV diffractometer of 285 mm radius in θ-θ geometry, using Cu*Kα* sealed-tube radiation (λ_{ave} = 1.5418 Å) operating at 40 kV and 30 mA. A diffracted-beam curved Ge monochromator, and NaI scintillation detector were used for data collection. The data, used for confirmation of phase purity and preliminary structural characterization of as-prepared samples, were collected at room temperature in the 2θ = 10° to 70° range in steps of 0.04° for 3 s. Data for Rietveld analysis at room temperature for all samples were collected in the 2θ = 10° to 120° range in steps of 0.02° for 10 s.

The as-prepared samples were also characterized through X-ray thermo-diffraction at the XPD-D10B beamline of the UVX ring of the Brazilian Synchrotron Light Laboratory (LNLS). The beamline was equipped with a θ–2θ reflection-geometry diffractometer with a Mythen-1000 linear position sensitive detector (PSD). Measurements were performed from RT to 500 °C in 100 °C steps in synthetic air atmosphere, similar to the catalytic conditions in the reactor (see below), using the in-house Canario furnace. X-rays with an energy of 10 keV (λ = 1.2372 Å) were used for data collection using a constant-monitor-counts strategy to determine the time of each step. The linear detector was scanned in 0.5° steps providing 6 measurements of each data point in one complete scan. Data reduction and averaging were carried out with the in-house software to obtain powder patterns in the 8° to 120° range with 0.005° 2θ-steps. The Rietveld method (as implemented in GSAS-II software suite [53]) was used to fit all X-ray powder diffraction data to confirm the desired phase formation, determine the phase composition and the structural parameters of the perovskite manganites.

4.2.3. Temperature-Programmed Reduction

Temperature Programmed Reduction was performed in a quartz reactor coupled to a TCD detector Autochem Micromeritics apparatus (TPR-TCD). 50 mg of catalysts were fed with a 5% H_2/Ar mixture at a flow rate of 60 $cm^3 \cdot min^{-1}$, with a heating rate of 10 $°C \cdot min^{-1}$. Prior to the temperature-programmed reduction (TPR) analysis, the sample was cleaned by heating up to 300 °C with a flow rate of 60 $cm^3 \cdot min^{-1}$ containing Ar, using a heating rate of 10 $°C \cdot min^{-1}$; then, the catalyst was kept for 1 h at 300 °C constant temperature and further cooled down to 25 °C under a continuous flow of Ar. The data obtained allow hydrogen consumption estimate for sample reduction in the range of temperature selected.

4.2.4. Temperature-Programmed Desorption

Temperature Programmed Desorption (TPD) was performed in a quartz reactor coupled to a quadrupole mass spectrometer (Pfeiffer, model Thermostar GSD301T1). A quantity of 200 mg of catalysts was fed with He, at a flow rate of 60 $cm^3 \cdot min^{-1}$, with a heating rate of 10 $°C \cdot min^{-1}$. Prior to the temperature-programmed desorption (TPD) analysis, the sample

was cleaned by heating up to 500 °C with a flow rate of 60 $cm^3 \cdot min^{-1}$ containing 100% O_2, using a heating rate of 10 °C·min^{-1}; then, the catalyst was kept for 1 h at 500 °C constant temperature, and further cooled down to 150 °C under a continuous flow of oxygen, and finally to 25 °C in He, except for $LaMnO_3$, which gains oxygen to form $LaMnO_{3+\delta}$ (similar to the calcined LM750 sample) at such conditions. This provides a semi-quantitative measure of the oxygen released from the sample.

4.2.5. Nitrogen Physisorption

Specific surface area (S_{BET}) measurements were performed applying the Brunauer-Emmett-Teller (BET) method to the nitrogen (Praxair, >99.95%) adsorption-desorption isotherms at −196 °C on outgassed samples for 10 h at 100 °C. The isotherms were recorded until relative pressures equal to 0.995 P_o using a Beckman Coulter SA3100 apparatus.

4.2.6. Scanning Electron Microscopy

The as-prepared and calcined samples were inspected at the micron scale by Scanning Electron Microscopy (SEM). Digital micrographs were acquired at 20 kV in a JEOL JS M-5900LV microscope. Elemental composition of selected areas of the samples was determined by means of an Energy Dispersive Spectrometry (EDS) probe (NORAN Instruments EDS-vantage probe).

4.2.7. X-ray Photoelectron Spectroscopy

X-ray photoelectron spectroscopy (XPS) measurements were performed using a SPECS system equipped with a PHOIBOS 150 1D-DLD hemispherical electron analyser. An Al-*Kα* (1486.6 eV, 150 W) X-ray source was used, and survey spectra were acquired with 50 eV pass energy, energy step size of 0.5 eV, and acquisition time of 0.1 s. For the high-resolution spectra, the analyser was adjusted to pass energy of 30 eV, an energy step size of 0.1 eV, and an acquisition time of 0.5 s. The Au $4f_{7/2}$ XPS peak obtained from a clean Au foil was applied for the analyser's energy calibration. An acceptance angle of $\pm 5°$ was used and the base pressure of the analysis chamber was 4×10^{-10} mbar. The spectra were analysed using the CasaXPS software and the charge was corrected considering the adventitious C 1 s chemical component (C-C, C-H) set to 284.5 eV binding energy. The fitting procedure also addressed the peaks line shape asymmetry considering a 20% Gauss-Lorentz ratio as well as Shirley-type background [54].

4.3. Catalytic Evaluation

Catalytic experiments were carried out in a quartz tubular reactor (diameter = 8 mm) with a "u" shape. For the tests, 0.5 g of catalyst was used. All catalysts were pressed into pellets at 5 MPa, crushed and sieved in order to obtain particle size between 425 μm and 600 μm, and prevent a pressure drop in the reactor. Additionally, the pre- and post-catalytic zones were filled with ground quartz to improve the homogeneity of the gaseous blend (avoiding the development of a laminar flux), both at the inlet and outlet of the catalytic fixed bed. A pre-treatment of the catalyst was performed at 300 °C for 1800 s in Ar flow. The reactivity of the samples was determined at atmospheric pressure, between 100 °C and 300 °C, in 50 °C steps with an Ar/O_2/Acetone reaction mixture (60 $cm^3 \cdot min^{-1}$, 3.42 $cm^3 \cdot min^{-1}$ and 1500 ppm_v, respectively). The O_2 gas flow goes through a saturator containing acetone (>99.5%, Dorwil), submerged in a water/ice bath (at 0.0 ± 0.1 °C) and the resulting mixture is diluted in Ar. Quantification of reagents and reaction products was accomplished by gas chromatography on a Shimadzu GC 2014, using a HAYESEP R 60/80 mesh column (diameter 1/8 mm SS, length 4.5 m) and TCD and FID detectors in series.

Consecutive catalytic cycles were carried out for all the as-prepared and LM750 samples under the same conditions without any sample treatment between cycles to assess the deactivation of the catalyst.

The acetone conversion was defined as:

$$Acetone\ Conversion\ (\%) = \frac{[\,Acet\,]_{in} - [\,Acet\,]_{out}}{[\,Acet\,]_{in}} \times 100$$

5. Conclusions

Samples of stoichiometric $LaMnO_3$, $La_{0.8}Ca_{0.2}MnO_3$, $La_{0.8}Sr_{0.2}MnO_3$ and $La_{0.8}Ba_{0.2}MnO_3$ perovskite manganites were prepared by an auto-combustion method. Additionally, cation-deficient $LaMnO_{3+\delta}$, $La_{0.8}Ca_{0.2}MnO_{3+\delta}$, $La_{0.8}Sr_{0.2}MnO_{3+\delta}$ and $La_{0.8}Ba_{0.2}MnO_{3+\delta}$ were obtained from them by calcination at 750 °C in air. The preparation method provides active samples in multi-gram batches with a simple procedure in a few hours of work. Structural characterization, behaviour against reduction, oxygen desorption, bulk and surface composition and textural measurements were conducted and tests for catalytic oxidation of acetone as a model VOC compound were performed. The results reveal that these single-phase perovskite manganites show good catalytic activity and remain active throughout the cycling both in the as-prepared and calcined forms, even though they present low BET areas and the presence of carbonates on the surface. The doping with larger alkaline earth cations such as Ba^{2+} and incorporation of extra oxygen in the structure by calcination seem to improve their activity. Both cation-size of the dopant and calcination seem to have synergistic effects, making calcined $La_{0.8}Ba_{0.2}MnO_{3+\delta}$ (LBM750) material the one with the largest acetone conversion at 200 °C. However, this improvement is insignificant at 300 °C where all the doped samples show acetone conversion above 95%. The change of alkaline earth metal in the perovskite changes the structure's bulk symmetry, increasing it from orthorhombic (Ca) to rhombohedral/cubic (Ba). This correlates with the improvement of activity with dopant size and with the equalization of the catalytic activity as the structural differences among samples are also reduced at 300 °C where all samples are rhombohedral or rhombohedral/cubic. The Mn^{4+}/Mn^{3+} ratio in the surface of the sample, accompanied by the high-symmetry cation-vacant bulk structure, seems to be more important than any other characteristics of the studied catalysts.

Supplementary Materials: The following supporting information can be downloaded at: https://www.mdpi.com/article/10.3390/catal12080865/s1, Figure S1: Rietveld fit of synchrotron XRD patterns of the as-prepared samples confirming the presence of pure manganites with perovskite structure (except for LCM that exhibits a 4.7% weight of $CaCO_3$ impurity). The LSM and LBM samples are mixtures of orthorhombic Pbnm and rhombohedral Rc perovskite phases. Figure S2: Rietveld fit of conventional XRD diffractograms of the calcined samples. Figure S3: Acetone conversion of LM750 over four consecutive cycles showing no sign of catalyst deactivation. Figure S4: $[CO_2]_{experimental}/[CO_2]_{theoretical}$ ratio vs. temperature curves for the as-prepared manganites and the calcined samples. Figure S5: Synchrotron XRD patterns of the indicated as-prepared samples heated from RT to 500 °C in air. The insets show in more detail the appearance/disappearance of some peaks during the heating process. Figure S6: N_2 physisorption isotherms for the indicated as-prepared and calcined samples. Figure S7: SEM images with EDS analysis corresponding to different zones of LM: (a) zone 1, (b) zone 2 and (c) zone 3. Figure S8: SEM images with EDS analysis corresponding to different zones of LM750: (a) zone 1, (b) zone 2 and (c) zone 3. Figure S9: SEM images with EDS analysis corresponding to different zones of LCM: (a) zone 1, (b) zone 2 and (c) zone 3. Figure S10: SEM images with EDS analysis corresponding to different zones of LCM750: (a) zone 1, (b) zone 2 and (c) zone 3. Figure S11: SEM images with EDS analysis corresponding to different zones of LSM: (a) zone 1, (b) zone 2 and (c) zone 3. Figure S12: SEM images with EDS analysis corresponding to different zones of LSM750: (a) zone 1, (b) zone 2 and (c) zone 3. Figure S13: SEM images with EDS analysis corresponding to different zones of LBM: (a) zone 1, (b) zone 2 and (c) zone 3. Figure S14: SEM images with EDS analysis corresponding to different zones of LBM750: (a) zone 1, (b) zone 2 and (c) zone 3. Figure S15: La $3d_{5/2}$ XPS spectra (dots) for all samples before and after the thermal treatments fitted with two chemical components, named La-OH (blue lines) and La-CO_3 (red lines), which present 3.9 and 3.5 eV splitting, respectively. Figure S16: Ca 2p, Sr 3d, and Ba $3d_{5/2}$ high-resolution XPS spectra (dots) acquired before and after the thermal treatments. Also shown are the corresponding chemical components indicated in the figure legends (blue and red lines). Table S1: ICP-AES spectroscopic results obtained for LM, LCM, LSM and LBM samples. Table S2:

Final parameters for the as-prepared samples XRD data obtained through Rietveld fit. Table S3: Atom % obtained by EDS corresponding to the points indicated in the different zones of the SEM images for the LM, LM750, LSM and LSM 750 samples. Table S4: Atom % obtained by EDS corresponding to the points indicated in the different zones of the SEM images for the LCM, LCM750, LBM and LBM 750 samples. Refs. [55,56] are cited in Supplementary Materials file.

Author Contributions: Conceptualization, C.D.l.S., L.S. and J.C.; methodology, C.D.l.S. and L.S.; formal analysis, C.D.l.S., H.V., J.M.G., L.S. and J.C.; investigation, N.D.B., C.D.l.S., M.D.P.Y., J.M., M.D.C.M.A. and A.A.; resources, J.M.G., L.S. and J.C.; data curation, C.D.l.S. and L.S.; writing—original draft preparation, N.D.B. and C.D.l.S.; writing—review and editing, C.D.l.S., H.V. and L.S.; supervision, C.D.l.S.; project administration, C.D.l.S. All authors have read and agreed to the published version of the manuscript.

Data Availability Statement: Not applicable.

Conflicts of Interest: The authors declare no conflict of interest.

References

1. Kim, H.-S.; Kim, H.-J.; Kim, J.-H.; Kim, J.-H.; Kang, S.-H.; Ryu, J.-H.; Park, N.-K.; Yun, D.-S.; Bae, J.-W. Noble-metal-based catalytic oxidation technology trends for volatile organic compound (VOC) removal. *Catalysts* **2022**, *12*, 63. [CrossRef]
2. Hou, Z.; Pei, W.; Zhang, X.; Zhang, K.; Liu, Y.; Deng, J.; Jing, L.; Dai, H. Rare earth oxides and their supported noble metals in application of environmental catalysis. *J. Rare Earths* **2020**, *38*, 819–839. [CrossRef]
3. Lee, J.E.; Ok, Y.S.; Tsang, D.C.W.; Song, J.H.; Jung, S.C.; Park, Y.K. Recent advances in volatile organic compounds abatement by catalysis and catalytic hybrid processes: A critical review. *Sci. Total Environ.* **2020**, *719*, 137405. [CrossRef] [PubMed]
4. Kamal, M.S.; Razzak, S.A.; Hossain, M.M. Catalytic oxidation of volatile organic compounds (VOCs)—A review. *Atmos. Environ.* **2016**, *140*, 117–134. [CrossRef]
5. Zang, M.; Zhao, C.; Wang, Y.; Chen, S. A review of recent advances in catalytic combustion of VOCs on perovskite-type catalysts. *J. Saudi Chem. Soc.* **2019**, *23*, 645–654. [CrossRef]
6. Li, W.B.; Wang, J.X.; Gong, H. Catalytic combustion of VOCs on non-noble metal catalysts. *Catal. Today* **2010**, *148*, 81–87. [CrossRef]
7. Ojala, S.; Koivikko, N.; Laitinen, T.; Mouammine, A.; Seelam, P.K.; Laassiri, S.; Ainassaari, K.; Rachid Brahmi, R.; Keiski, R.L. Utilization of volatile organic compounds as an alternative for destructive abatement. *Catalysts* **2015**, *5*, 1092–1151. [CrossRef]
8. Spinicci, R.; Faticanti, M.; Marini, P.; De Rossi, S.; Porta, P. Catalytic activity of $LaMnO_3$ and $LaCoO_3$ perovskites towards VOCs combustion. *J. Mol. Catal. A Chem.* **2003**, *197*, 147–155. [CrossRef]
9. Kim, S.C.; Shim, W.G. Catalytic combustion of VOCs over a series of manganese oxide catalysts. *Appl. Catal. B Environ.* **2010**, *98*, 180–185. [CrossRef]
10. Rezlescu, N.; Rezlescu, E.; Popa, P.D.; Doroftei, C.; Ignat, M. Partial substitution of manganese with cerium in $SrMnO_3$ nano-perovskite catalyst. Effect of the modification on the catalytic combustion of dilute acetone. *Mater. Chem. Phys.* **2016**, *182*, 332–337. [CrossRef]
11. Yang, J.; Li, L.; Yang, X.; Song, S.; Li, J.; Jing, F.; Chu, W. Enhanced catalytic performances of in situ-assembled $LaMnO_{3/\delta}$-MnO_2 hetero-structures for toluene combustion. *Catal. Today* **2019**, *327*, 19–27. [CrossRef]
12. Doroftei, C.; Popa, P.D.; Rezlescu, E.; Rezlescu, N. Nanocrystalline $SrMnO_3$ powder as catalyst for hydrocarbon combustion. *J. Alloys Compd.* **2014**, *584*, 195–198. [CrossRef]
13. Hammami, R.; Ben Aissa, S.; Batis, H. Effects of thermal treatment on physico-chemical and catalytic properties of lanthanum manganite $LaMnO_{3+y}$. *Appl. Catal. A Gen.* **2009**, *353*, 145–153. [CrossRef]
14. Peña, M.A.; Fierro, J.L.G. Chemical structures and performance of perovskite oxides. *Chem. Rev.* **2017**, *101*, 1981–2017. [CrossRef] [PubMed]

15. Santos, V.P.G.; Santos, M.S.; Resini, C.; Brandão, S.T. Síntese e caracterização de perovskitas LaMnO$_3$ e γ-alumina como catalisadores para a reação de combustão do metano. *Matéria* **2017**, *22*, e-11913. [CrossRef]

16. Zhu, H.; Zhang, P.; Dai, S. Recent advances of lanthanum-based perovskite oxides for catalysis. *ACS Catal.* **2015**, *5*, 6370–6385. [CrossRef]

17. Marti, P.E.; Baiker, A. Influence of the A-site cation in AMnO$_{3+x}$ and AFeO$_{3+x}$ (A=La, Pr, Nd and Gd) perovskite-type oxides on the catalytic activity for methane combustion. *Catal. Lett.* **1994**, *26*, 71–84. [CrossRef]

18. Liu, Y.; Dai, H.; Du, Y.; Deng, J.; Zhang, L.; Zhao, Z.; Au, C.T. Controlled preparation and high catalytic performance of three-dimensionally ordered macroporous LaMnO$_3$ with nanovoid skeletons for the combustion of toluene. *J. Catal.* **2012**, *287*, 149–160. [CrossRef]

19. Liu, Y.; Dai, H.; Deng, J.; Du, Y.; Li, X.; Zhao, Z.; Wang, Y.; Gao, B.; Yang, H.; Guo, G. In situ poly(methyl methacrylate)-templating generation and excellent catalytic performance of MnO$_x$/3DOM LaMnO$_3$ for the combustion of toluene and methanol. *Appl. Catal. B Environ.* **2013**, *140–141*, 493–505. [CrossRef]

20. Zhang, C.; Guo, Y.; Guo, Y.; Lu, G.; Boreave, A.; Retailleau, L.; Baylet, A.; Giroir-Fendler, A. Environmental LaMnO$_3$ perovskite oxides prepared by different methods for catalytic oxidation of toluene. *Appl. Catal. B Environ.* **2014**, *148–149*, 490–498. [CrossRef]

21. Einaga, H.; Hyodo, S.; Teraoka, Y. Complete oxidation of benzene over perovskite-type oxide catalysts. *Top. Catal.* **2010**, *53*, 629–634. [CrossRef]

22. Miniajluk, N.; Trawczyński, J.; Zawadzki, M. Properties and catalytic performance for propane combustion of LaMnO$_3$ prepared under microwave-assisted glycothermal conditions: Effect of solvent diols. *Appl. Catal. A Gen.* **2017**, *531*, 119–128. [CrossRef]

23. Ding, Y.; Wang, S.; Zhang, L.; Chen, Z.; Wang, M.; Wang, S. A facile method to promote LaMnO$_3$ perovskite catalyst for combustion of methane. *Catal. Commun.* **2017**, *97*, 88–92. [CrossRef]

24. Padilla, O.; Munera, J.; Gallego, J.; Santamaria, A. Approach to the characterization of monolithic catalysts based on la perovskite-like oxides and their application for VOC oxidation under simulated indoor environment conditions. *Catalysts* **2022**, *12*, 168. [CrossRef]

25. Zhang, C.; Wang, C.; Zhan, W.; Guo, Y.; Guo, Y.; Lu, G.; Baylet, A.; Giroir-Fendler, A. Catalytic oxidation of vinyl chloride emission over LaMnO$_3$ and LaB$_{0.2}$Mn$_{0.8}$O$_3$ (B=Co, Ni, Fe) catalysts. *Appl. Catal. B Environ.* **2013**, *129*, 509–516. [CrossRef]

26. Zhang, C.; Cao, H.; Wang, C.; He, M.; Zhan, W.; Guo, Y. Catalytic mechanism and pathways of 1, 2-dichloropropane oxidation over LaMnO$_3$ perovskite: An experimental and DFT study. *J. Hazard. Mater.* **2021**, *402*, 123473. [CrossRef]

27. Yang, L.; Li, Y.; Sun, Y.; Wang, W.; Shao, Z. Perovskite oxides in catalytic combustion of volatile organic compounds: Recent advances and future prospects. *Energy Environ. Mater.* **2021**, 1–26. [CrossRef]

28. Wold, A.; Arnott, R.J. Preparation and crystallographic properties of the systems LaMn$_{l-x}$Mn$_x$O$_{3+\lambda}$ and LaMn$_{1-x}$Ni$_x$O$_{3+\lambda}$ JA-1106. *J. Phys. Chem. Solids* **1959**, *9*, 176–180. [CrossRef]

29. Alonso, J.A.; Martínez-Lope, M.J.; Casáis, M.T.; Muñoz, A. Magnetic structures of LaMnO$_{3+\delta}$ perovskites (δ = 0.11, 0.15, 0.26). *Solid State Commun.* **1997**, *102*, 7–12. [CrossRef]

30. Topfer, J.; Goodenough, J.B. LaMnO$_{3+\delta}$ revisited. *J. Solid State Chem.* **1997**, *130*, 117–128. [CrossRef]

31. Mitchell, J.F.; Argyriou, D.N.; Potter, C.D.; Hinks, D.G.; Jorgensen, J.D.; Bader, S.D. Structural phase diagram of La$_{1-x}$Sr$_x$MnO$_{3+\delta}$: Relationship to magnetic and transport properties. *Phys. Rev. B* **1996**, *54*, 6172–6183. [CrossRef] [PubMed]

32. Pan, K.L.; Pan, G.T.; Chong, S.; Chang, M.B. Removal of VOCs from gas streams with double perovskite-type catalysts. *J. Environ. Sci.* **2018**, *69*, 205–216. [CrossRef] [PubMed]

33. Stege, W.P.; Cadús, L.E.; Barbero, B.P. La$_{1-x}$Ca$_x$MnO$_3$ perovskites as catalysts for total oxidation of volatile organic compounds. *Catal. Today* **2011**, *172*, 53–57. [CrossRef]

34. Wang, L.; Wang, C.; Xie, H.; Zhan, W.; Guo, Y.; Guo, Y. Catalytic combustion of vinyl chloride over Sr doped LaMnO$_3$. *Catal. Today* **2019**, *327*, 190–195. [CrossRef]

35. Mitchell, R.H. *Perovskites: Modern and Ancient*; Almaz Press Inc.: Thunder Bay, ON, Canada, 2002.

36. Yang, C.; Grimaud, A. Factors controlling the redox activity of oxygen in perovskites: From theory to application for catalytic reactions. *Catalysts* **2017**, *7*, 149. [CrossRef]

37. Vázquez, S.; Basbus, J.; Soldati, A.L.; Napolitano, F.; Serquis, A.; Suescun, L. Effect of the symmetric cell preparation temperature on the activity of Ba$_{0.5}$Sr$_{0.5}$Fe$_{0.8}$Cu$_{0.2}$O$_{3-\delta}$ as cathode for intermediate temperature solid oxide fuel cells. *J. Power Sources* **2015**, *274*, 318–323. [CrossRef]

38. Cui, W.; Chen, H.; Liu, Q.; Cui, M.; Chen, X.; Fei, Z. Mn/Co redox cycle promoted catalytic performance of mesoporous SiO$_2$-confined highly dispersed LaMn$_x$Co$_{1-x}$O$_3$ perovskite oxides in n-butylamine combustion. *Chem. Sel.* **2020**, *5*, 8504–8511.

39. Esmaeilnejad-Ahranjani, P.; Khodadadi, A.A.; Mortazavi, Y. Self-regenerative function of Cu in LaMnCu$_{0.1}$O$_3$ catalyst: Towards noble metal-free intelligent perovskites for automotive exhaust gas treatment. *Appl. Catal. A Gen.* **2020**, *602*, 117702. [CrossRef]

40. Zhang, C.; Zeng, K.; Wang, C.; Liu, X.; Wu, G.; Wang, Z.; Wang, D. LaMnO$_3$ perovskites via a facile nickel substitution strategy for boosting propane combustion performance. *Ceram. Int.* **2020**, *46*, 6652–6662. [CrossRef]

41. Gu, H.; Yang, G.; Hu, Y.; Liang, M.; Chen, S.; Ran, R.; Xu, M.; Wang, W.; Zhou, W.; Shao, Z. Enhancing the oxygen reduction activity of PrBaCo$_2$O$_{5+\delta}$ double perovskite cathode by tailoring the calcination temperatures. *Int. J. Hydrog. Energy* **2020**, *45*, 25996–26004. [CrossRef]

42. Moulder, J.F.; Stickle, W.F.; Sohol, P.E.; Bomben, K.D. *Handbook of X-ray Photoelectron Spectroscopy*; Perkin-Elmer Corporation, Physical Electronics Inc.: Eden Prairie, MN, USA, 1992.

43. Østergaard, M.B.; Strunck, A.B.; Boffa, V.; Jørgensen, M.K. Kinetics of strontium carbonate formation on a Ce-doped SrFeO$_3$ perovskite. *Catalysts* **2022**, *12*, 265. [CrossRef]

44. Feldhoff, A.; Martynczuk, J.; Wang, H. Advanced Ba$_{0.5}$Sr$_{0.5}$Zn$_{0.2}$Fe$_{0.8}$O$_{3-\delta}$ perovskite-type ceramics as oxygen selective membranes: Evaluation of the synthetic process. *Prog. Solid State Chem.* **2007**, *35*, 339–353. [CrossRef]

45. Chattaraj, B.D.; Dutta, S.N.; Iyengar, M.S. Studies on the thermal decomposition of calcium carbonate in the presence of alkali salts (Na$_2$CO$_3$, K$_2$CO$_3$ and NaCl). *J. Therm. Anal.* **1973**, *5*, 43–49. [CrossRef]

46. Foger, K.; Hoang, M.; Turney, T.W. Formation and thermal decomposition of rare-earth carbonates. *J. Mater. Sci.* **1992**, *27*, 77–82. [CrossRef]

47. Alvero, R.; Odriozola, J.A.; Trillo, J.M. Lanthanide oxides: Preparation and ageing. *J. Chem. Soc. Dalton Trans.* **1984**, *2*, 87–91. [CrossRef]

48. Arai, H.; Yamada, T.; Eguchi, K.; Seiyama, T. Catalytic combustion of methane over various perovskite-type oxides. *Appl. Catal.* **1986**, *26*, 265–276. [CrossRef]

49. Alami, D. Environmental applications of rare-earth manganites as catalysts: A comparative study. *Environ. Eng. Res.* **2013**, *4*, 211–219. [CrossRef]

50. Bellakki, M.B.; Shivakumara, C.; Vasanthacharya, N.Y.; Prakash, A.S. Rapid synthesis of room temperature ferromagnetic ag-doped LaMnO$_3$ perovskite phases by the solution combustion method. *Mater. Res. Bull.* **2010**, *45*, 1685–1691. [CrossRef]

51. Vázquez, S.; Davyt, S.; Basbus, J.F.; Soldati, A.L.; Amaya, A.; Serquis, A.; Faccio, R.; Suescun, L. Synthesis and characterization of La$_{0.6}$Sr$_{0.4}$Fe$_{0.8}$Cu$_{0.2}$O$_{3-\delta}$ oxide as cathode for intermediate temperature solid oxide fuel cells. *J. Solid State Chem.* **2015**, *228*, 208–213. [CrossRef]

52. Grassi, J.; Macias, M.A.; Castiglioni, J.; Basbus, J.F.; Gauthier, G.H.; Serquis, A.; Suescun, L. Synthesis, characterization of high temperature properties and evaluation of YBa$_2$Cu$_3$O$_{6+\delta}$ as cathode for Intermediate Temperature Solid Oxide Fuel Cells. *J. Mater. Sci. Technol. Res.* **2021**, *8*, 81–92. [CrossRef]

53. Toby, B.H.; Von Dreele, R.B. GSAS-II: The genesis of a modern open-source all purpose crystallography software package. *Appl. Crystallogr.* **2013**, *46*, 544–549. [CrossRef]

54. Shirley, D.A. High-resolution X-ray photoemission spectrum of the valence bands of gold. *Phys. Rev. B* **1972**, *5*, 4709–4714. [CrossRef]

55. Sunding, M.F.; Hadidi, K.; Diplas, S.; Lovvik, O.M.; Norby, T.E.; Gunnaes, A.E. XPS characterization of in situ treated lanthanum oxide and hydroxide using tailored charge referencing and peak fitting procedures. *J. Electron Spectrosc. Related Phenom.* **2011**, *184*, 399–409.

56. Li, J.P.H.; Zhou, X.; Pang, Y.; Zhu, L.; Vovk, E.I.; Cong, L.; van Bavel, A.P.; Li, S.; Yang, Y. Understanding of binding energy calibration in XPS of lanthanum oxide by in situ treatment. *Phys. Chem. Chem. Phys.* **2019**, *21*, 22351.